AGU PUBLICATIONS

Geophysical Research Letters

RESEARCH LETTER

10.1002/2015GL063601

Key Points:
- Reconnection electric and normal magnetic fields heat meandering electrons
- Distributions evolve spatially and temporally near and after peak reconnection
- Triangular, striated distributions can identify the electron diffusion region

Correspondence to:
J. R. Shuster,
jrf63@wildcats.unh.edu

Citation:
Shuster, J. R., L.-J. Chen, M. Hesse, M. R. Argall, W. Daughton, R. B. Torbert, and N. Bessho (2015), Spatiotemporal evolution of electron characteristics in the electron diffusion region of magnetic reconnection: Implications for acceleration and heating, *Geophys. Res. Lett.*, *42*, 2586–2593, doi:10.1002/2015GL063601.

Received 23 FEB 2015
Accepted 23 MAR 2015
Accepted article online 28 MAR 2015
Published online 22 APR 2015

Spatiotemporal evolution of electron characteristics in the electron diffusion region of magnetic reconnection: Implications for acceleration and heating

J. R. Shuster[1], L.-J. Chen[2], M. Hesse[2], M. R. Argall[1], W. Daughton[3], R. B. Torbert[1], and N. Bessho[2]

[1]Space Science Center, University of New Hampshire, Durham, New Hampshire, USA, [2]NASA Goddard Space Flight Center, Greenbelt, Maryland, USA, [3]Los Alamos National Laboratory, Los Alamos, New Mexico, USA

Abstract Based on particle-in-cell simulations of collisionless magnetic reconnection, the spatiotemporal evolution of electron velocity distributions in the electron diffusion region (EDR) is reported to illustrate how electrons are accelerated and heated. Approximately when the reconnection rate maximizes, electron distributions in the vicinity of the X line exhibit triangular structures with discrete striations and a temperature (T_e) twice that of the inflow region. T_e increases as the meandering EDR populations mix with inflowing electrons. As the distance from the X line increases within the electron outflow jet, the discrete populations swirl into arcs and gyrotropize by the end of the jet with T_e about 3 times that of the X line. Two dominant processes increase T_e and produce the spatially and temporally evolving EDR distributions: (1) electric field acceleration preferential to electrons which meander in the EDR for longer times and (2) cyclotron turning by the magnetic field normal to the reconnection layer.

1. Introduction

How can magnetic reconnection occur in a collisionless plasma? The electron diffusion region (EDR) is believed to hold the key to this question. The reconnection electric field has been assumed to heat inflowing plasma and drive intense currents in the EDR [*Hesse et al.*, 2009]. This paper elucidates how the reconnection electric field contributes to electron heating in the EDR. Throughout this paper, heating refers to increases of the electron temperature T_e defined as $\mathrm{Tr}(P_e)/3n_e$, where $\mathrm{Tr}(P_e)$ is the trace of the electron pressure tensor and n_e the electron density.

Several studies have shown that for antiparallel reconnection, transport of the out-of-plane (y) electron momentum to the outflow (x) direction is the main mechanism that limits the current density and provides the resistivity for reconnection to occur [*Lyons and Pridmore-Brown*, 1990; *Cai et al.*, 1994; *Fujimoto and Sydora*, 2009; *Hesse et al.*, 2009; *Chen et al.*, 2011], supporting the concept of inertia resistivity [*Speiser*, 1970; *Hesse et al.*, 2011]. Anomalous resistivity due to scattering of electrons by wave fluctuations has also been proposed for limiting the out-of-plane current density as well as heating electrons (see the review paper by *Hesse et al.* [2011], and references therein). A recent mechanism that has received much attention in simulation and space observation communities involves a parallel electric potential to accelerate electrons up to the edge of EDR and to determine the shoulder energy of flat-top exhaust electron distributions and hence the amount of heating [*Egedal et al.*, 2010, 2012]. Through examination of the spatiotemporal evolution of electron distributions as discussed in this paper, we show that heating in the EDR is mainly accomplished by the combination of electric field acceleration and cyclotron turning.

The electron velocity distributions within a few electron skin depths of the X line have been shown to exhibit a triangular shape with discrete striations by using test particle tracing and Liouville mapping given a prescribed inflow distribution [*Ng et al.*, 2011, 2012] and by employing particle-in-cell simulations [*Ng et al.*, 2012; *Bessho et al.*, 2014]. The EDR and the exhaust are thought to be nearly isotropic for weak guide fields (less than 10% of the reconnecting component) based on the ratio of the pressure components parallel and perpendicular to the magnetic field [*Le et al.*, 2013]. *Shuster et al.* [2014] show highly structured anisotropic electron distributions in the exhaust, including arc and ring populations, which develop at around the time when the peak reconnection rate occurs. The discrete arc and ring structures are formed by electrons accelerated in the EDR and turned by the normal component of the magnetic field, B_z [*Bessho et al.*, 2014], which

©2015. American Geophysical Union. All Rights Reserved.

increases downstream of the X line. In the reconnection layer, the increasing $|B_z|$ turns the y momenta of accelerated electrons to the x (outflow) direction to form jets and limit the out-of-plane current [*Hesse et al.*, 2009; *Chen et al.*, 2011], transfers part of the incoming parallel energy to perpendicular energy [*Ng et al.*, 2011], and converts bulk kinetic energy into thermal energy by gyrotropizing distributions, as will be discussed below.

2. Simulation Setup

We employ particle-in-cell simulations with two spatial and three velocity dimensions. The initial conditions contain a Harris sheet with unperturbed magnetic field component $B_x = B_0 \tanh(z/L)$, where B_0 is the asymptotic value of the magnetic field and $L = 0.5d_i$ (d_i is the ion skin depth based on the Harris sheet density n_0) is the half width of the current sheet. The density profile is $n(z) = n_0 \mathrm{sech}^2(z/L) + n_b$, where $n_b/n_0 = 0.05$ is the background density. The domain is $L_x \times L_z = 80d_i \times 20d_i$ with open boundary conditions in x and z. Other Harris sheet plasma parameters are the electron plasma to cyclotron frequency ratio $\omega_{pe}/\Omega_{ce} = 2$, ion to electron temperature ratio $T_i/T_e = 5$, background to current sheet temperature ratio $T_b/T_0 = 0.333$, and ion to electron mass ratio $m_i/m_e = 400$. Reconnection is initiated by adding a perturbation in the magnetic field [*Daughton et al.*, 2006]. Two runs are performed with the initial guide field $B_g = 0$ and $0.03B_0$, respectively, while keeping all other parameters the same. Each run uses $10{,}240 \times 2560$ cells with an average of 600 particles per cell per species. The results from the two runs pertaining to the spatiotemporal evolution of electron distributions agree qualitatively. Only data from the zero guide field run are presented. Throughout the paper, unless otherwise noted, velocities are in units of V_A, the Alfvén speed defined by B_0 and n_0; lengths in d_e, the electron skin depth using n_0; and time in Ω_{ci}^{-1}, the inverse ion cyclotron frequency based on B_0.

3. Simulation Results

Here we discuss the spatiotemporal evolution of electron velocity distributions and what we can learn about electron acceleration and heating in the EDR. The spatial evolution of the distributions upstream of, within, and downstream of the EDR at $t\Omega_{ci} = 19$ (about one Ω_{ci}^{-1} from the time when the reconnection rate peaks—see *Shuster et al.* [2014] for the reconnection rate time profile) is presented in Figure 1. An overview of the outflow jet U_{ex} and its one-dimensional cut along $z = 0$ are displayed in Figure 1a. Five electron distributions are taken from the EDR locations marked with white boxes in the U_{ex} 2-D plot and displayed in Figure 1b in v_x-v_y (distributions 1A–5A), v_x-v_z (1B–5B), and v_z-v_y (1C–5C) velocity space, respectively.

The electron distribution at the X line exhibits a distinct triangular shape with discrete striations shifted in $-v_y$ (distribution 1A). This feature is consistent with previous reports [*Ng et al.*, 2011, 2012; *Bessho et al.*, 2014], but the number of discernible striations differ, indicating the robustness of the triangular shape and the striation's sensitivity to plasma parameters (such as those of the initial current sheet). The discrete striations in distribution 1(A–C) result from the oscillatory out-of-plane force $F_y = -eE_y - ev_zB_x$ on meandering (oscillatory v_z) electrons [*Bessho et al.*, 2014], where e is the elementary charge and E_y is the reconnection electric field. The oscillations in F_y lead to steps in v_y and hence discrete regions of enhanced phase-space densities in the v_y dimension of the distributions, such as distributions 1A and 1C.

The formation of the triangular distribution highlights the cause of EDR heating from upstream to the X line. The first striation in distribution 1A is formed by electrons entering the EDR and arriving at the X line without any bounces in z [*Ng et al.*, 2011; *Bessho et al.*, 2014]. Comparing this first striation to the inflow distribution shown in grey in the same panel (taken from the grey box $6d_e$ above the X line), we observe a shift in $-v_y$ and a slight decrease in the v_x width. Electrons in the higher-order striations undergo more bounces in the EDR and experience more E_y acceleration and more conversion to v_y from v_x by B_z. A triangular distribution is thus formed in the vicinity of the X line, since higher-order striations are further shifted in $-v_y$ as well as narrower in v_x widths. The mixing of electrons spending different amounts of time in the EDR and thus receiving different amounts of acceleration leads to an abrupt increase of T_e as will be further discussed and shown in Figures 2 and 4.

Two main populations in distributions 1B–3B reside at $v_z > 0$ and $v_z < 0$, consistent with the electron phase-space hole in the z-v_z space due to the meandering oscillations of electrons under finite reconnection inflow reported by *Chen et al.* [2011]. The average $|v_z|$ of both populations is larger than the maximum electron inflow speed (roughly the center v_z of the grey inflow distribution shown in distributions 1B and 1C)

©2015. American Geophysical Union. All Rights Reserved.

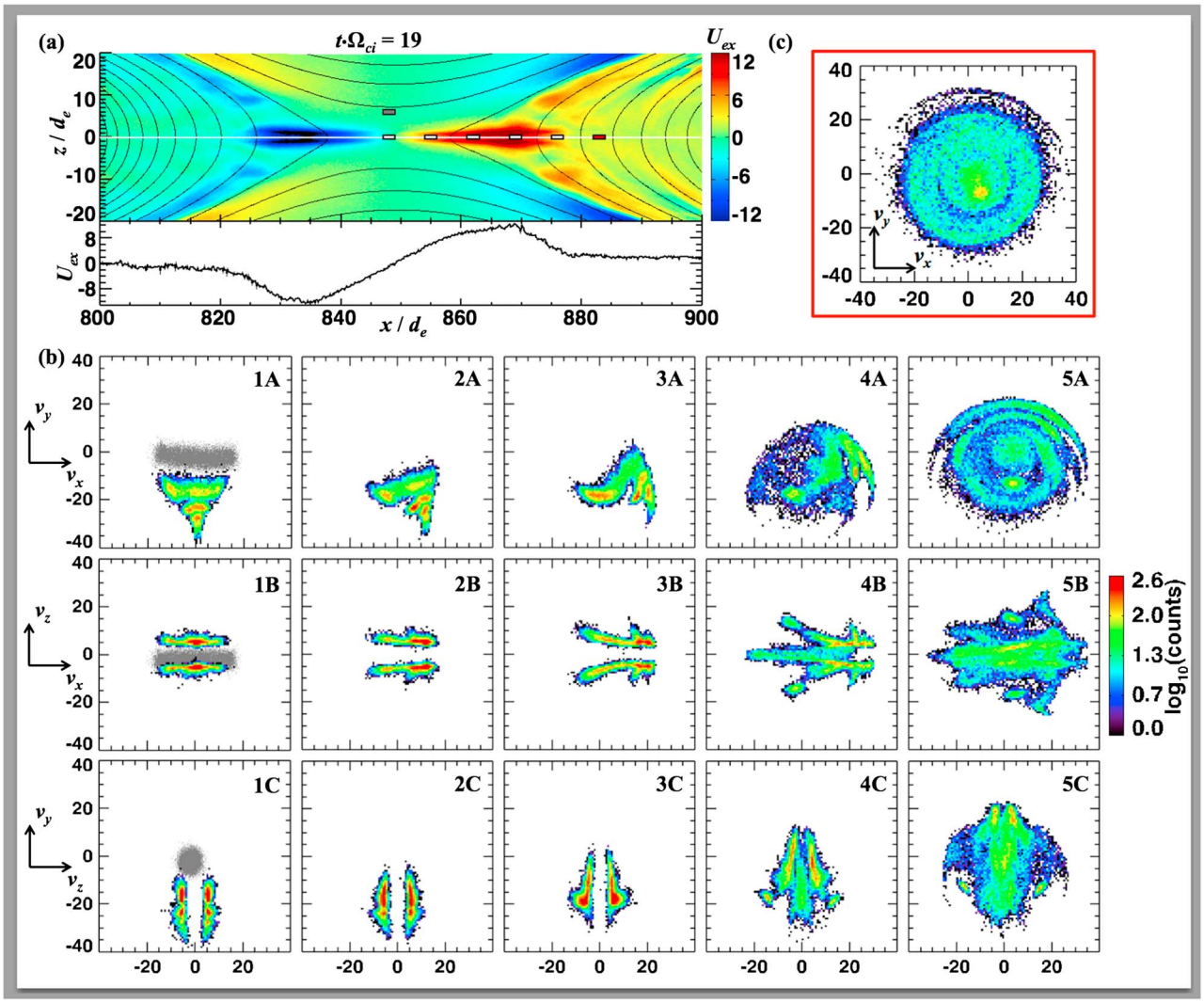

Figure 1. Electron velocity distributions in and near the EDR revealing how electrons are heated downstream as the discrete, striated populations at the X line rotate and spread out in gyrophase. (a) Electron outflow jet U_{ex} and its 1-D cut along $z = 0$ providing the spatial context for the distributions. (b) Projections in v_x-v_y (1–5)A, v_x-v_z (1–5)B, and v_z-v_y (1–5)C space of the EDR distributions taken from the five white bins in Figure 1a. The upstream inflow distribution taken from the grey bin at $z = 6$ in Figure 1a is overlaid in grey on the X line distribution 1(A–C) to visually illustrate the amount of acceleration and heating achieved in the EDR. Distribution 1(A–C) at the X line consists of two triangular lobes, each with discrete striations. (c) The v_x-v_y distribution taken from the red bin at $x = 883$ ($7d_e$ downstream from distribution 5) is almost fully gyrotropized and has a T_e larger than distribution 5. (All distributions are made using a spatial bin size of $2d_e \times 1d_e$.)

because the electrons have been accelerated by the inversion electric field E_z that self-consistently supports the electron phase-space hole structure. When the inversion E_z is insignificant (such as at the edge of the EDR or at later phases of reconnection), each of the two v_z populations is roughly centered at the respective maximum inflow electron fluid velocity (see distribution J in Figure 4b, for example), resulting in an increase of $T_{ezz} = P_{ezz}/n_e$.

Heating in the EDR downstream of the X line can be seen by comparing distributions 1A–5A and the distribution in Figure 1c (taken from the red bin shown in Figure 1a). The populations accelerated in $-y$ acquire $+v_x$ (2A–4A), and then further rotate toward $+v_y$ and $-v_x$ (4A and 5A) as electrons perform partial cyclotron orbits due to B_z. Arc and spiral structures are formed (best seen in v_x-v_y, distributions 3A–5A) before the distribution is subsequently gyrotropized (Figure 1c). The v_x-v_y spread (which is approximately $T_{e\perp} = (P_{exx} + P_{eyy})/2n_e$ since the magnetic field in the $z = 0$ plane is mainly along z) increases from the X line (distribution 1A) to just beyond the end of the jet (Figure 1c). This increase of $T_{e\perp}$ will be shown quantitatively in Figure 4a.

©2015. American Geophysical Union. All Rights Reserved.

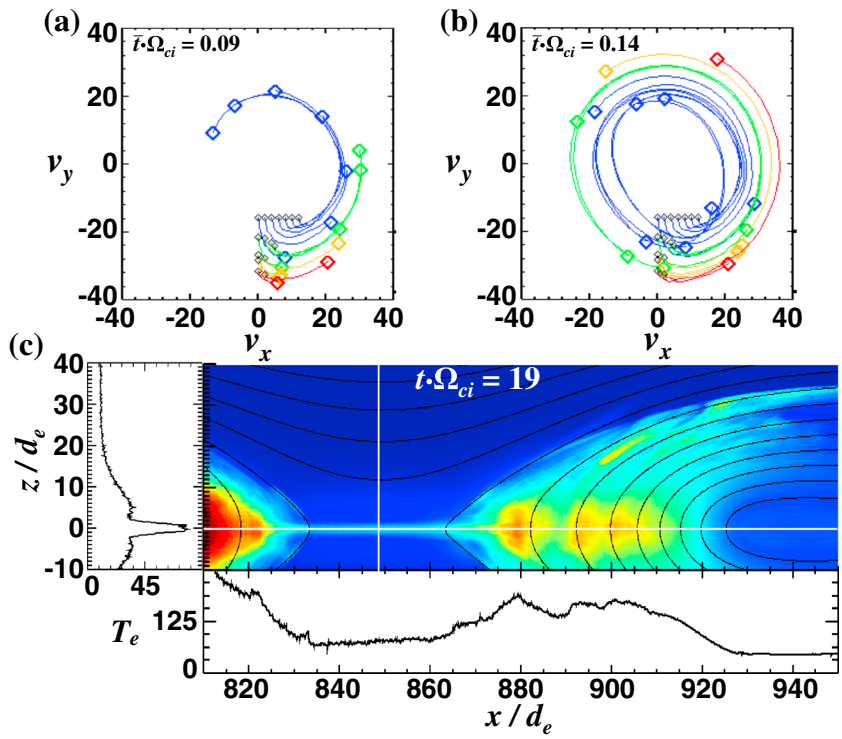

Figure 2. Electron trajectories illustrating how electrons are heated downstream from the X line and the electron temperature profile showing the amount of heating. (a and b) v_x-v_y trajectories of electrons from the first, second, third, and fourth striations in distribution 1A (Figure 1b) are colored blue, green, orange, and red, respectively. Small black diamonds mark the initial velocities of the traced particles, while the large colored diamonds mark the velocities of electrons at the elapsed particle tracing time, $\bar{t}$ ($\bar{t}\Omega_{ci} = 0.09$ in Figure 2a, and $\bar{t}\Omega_{ci} = 0.14$ in Figure 2b). The trajectories show how the electrons spread out in gyrophase as they flow downstream and perform partial cyclotron orbits in the increasing B_z. Thus, the initial bulk velocity in $-y$ is converted to the thermal energy, leading to an increase of $T_{e\perp}$. (c) The electron temperature, T_e, increases by approximately $4T_{e0}$ going from just upstream of the EDR ($z \sim 6$) to the X line ($z \sim 0$) and increases again by almost $12T_{e0}$ going from the X line ($x \sim 848$) to the end of the outflow jet ($x \sim 880$), where T_{e0} is the electron temperature far upstream at $z = 40$.

Cyclotron turning by B_z converts the electron's bulk velocity (directed mainly in the $-y$ direction at the X line) into thermal energy by spreading out electrons' gyrophases, as shown in the v_x-v_y distributions of Figure 1. To further illustrate this process, we present results from particle tracing using the E and B fields from $t\Omega_{ci} = 19$ in Figure 2. Representative electrons from each striation are traced forward in time starting from the initial velocities marked with small black diamonds shown in Figures 2a and 2b. The trajectories of the traced electrons in v_x-v_y space are displayed and color coded to distinguish their originating striations. Figure 2a shows the tracing results up to $\bar{t}\Omega_{ci} = 0.09$ ($\bar{t}\omega_{pe} = 76.16$), and Figure 2b the results up to $\bar{t}\Omega_{ci} = 0.14$ ($\bar{t}\omega_{pe} = 112.83$), where $\bar{t}$ is time in the particle tracing simulation. The large colored diamonds in Figure 2a (Figure 2b) indicate the electron velocities at $\bar{t}\Omega_{ci} = 0.09$ ($\bar{t}\Omega_{ci} = 0.14$).

The selected electrons spread out further in gyrophase as $\bar{t}$ advances. Electrons starting with larger v_x (such as the electron marked with a blue diamond from the first striation that has already completed ~3/4 of a gyration in Figure 2a) travel faster downstream and encounter the stronger B_z before electrons that started with smaller v_x. Electrons starting with $v_x = 0$ (leftmost of the initial black diamonds) remain in the vicinity of the X line the longest and thus have been accelerated by E_y the most, which can be seen visually in Figure 2a: the $v_x = 0$ electrons in each striation have gained the most $|v_y|$ compared to the other electrons at this time. Both the blue and green electrons have acquired more $|v_y|$ after completing their first gyration (Figure 2b), as E_y acceleration continues to occur during the cyclotron turning until electrons are remagnetized. The large bulk velocity $-v_y$ near the X line is converted into thermal velocity perpendicular to B_z as electrons travel downstream, resulting in an increased $T_{e\perp}$. Consequently, T_e is increased, since $T_{e\parallel} \sim T_{ezz}$ does not change appreciably from the X line to the end of the electron jet (see the v_z spreads in distributions (1–5)B and (1–5)C).

©2015. American Geophysical Union. All Rights Reserved.

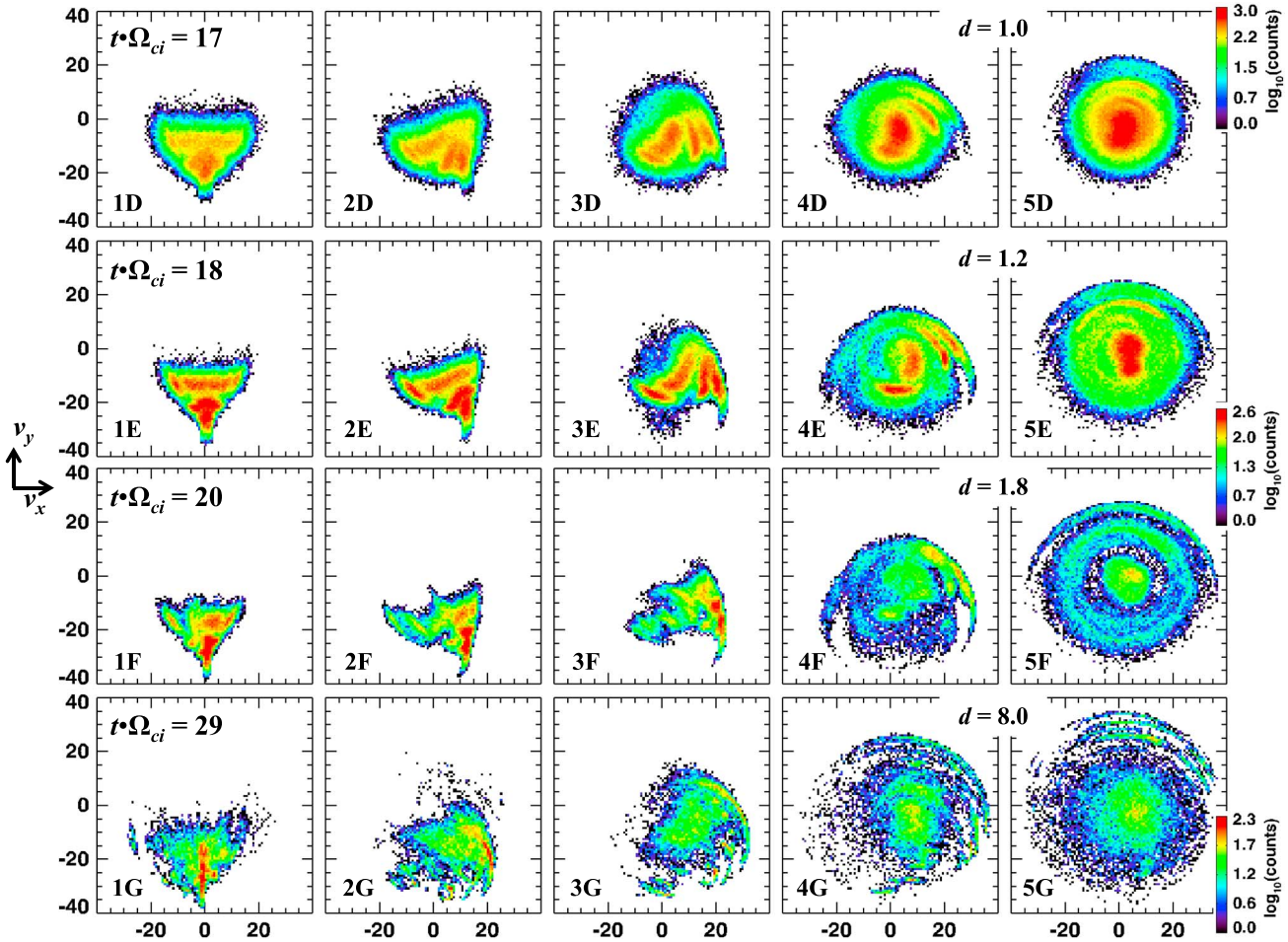

Figure 3. Spatial and temporal evolution of electron distributions in v_x-v_y space from the X line to the end of the electron outflow jet (horizontal) for $t\Omega_{ci} = 17$, 18, 20, and 29 (vertical). All distributions are made using a spatial bin size of $2d_e \times 2d_e$. As the electron current layer lengthens, the end of the electron outflow jet is stretched farther away from the X line and is given by the number d (in d_i), which measures the distance from the X line to the location where distribution 5 is taken. For $t\Omega_{ci} = 17$ and 18, the spatial evolution of the distributions is similar to those shown in Figure 1b. Further in time, the triangular shape of the X line distributions remains, though the striations become fragmented. Arcs are found near the end of the electron jet for $t\Omega_{ci} \geq 17$.

The amount of temperature increase from the inflow to the X line and to near the end of the electron jet can be seen in Figure 2c, where T_e in units of $m_e V_A^2$ is displayed. Notice that $T_e = 10.3 = T_{e0}$ at $z/d_e = 40$ (upstream of the ion diffusion region), rises to $3.3T_{e0}$ at $z/d_e = 6$ (upstream and just outside of the EDR) over a few tens of d_e, abruptly increases to $7.4T_{e0}$ at $(x, z) = (848, 0)$ (X line) within a few d_e, and further grows to $19.3T_{e0}$ near $(x, z) = (880, 0)$ (just beyond the end of the electron jet). The T_e increase of $16T_{e0}$ from just upstream to downstream of the EDR is a combined effect of E_y acceleration and cyclotron turning by B_z, while the T_e increase of $2.3T_{e0}$ upstream from the EDR is mainly due to acceleration by the parallel electric field [*Chen et al.*, 2009; *Egedal et al.*, 2010]. T_e further downstream does not surpass the T_e near the end of the electron outflow jet ($z \sim 880$). Note that the sharp rise in T_e on the $-x$ side of the X line ($x < 820$) is associated with highly anisotropic ($T_{e\perp} > T_{e\parallel}$) ring distributions discussed in *Shuster et al.* [2014].

The time evolution of the distributions in the v_x-v_y space from the X line to the end of the electron outflow jet is shown in Figure 3. The time range is $t\Omega_{ci} = 17$ (one Ω_{ci}^{-1} before the time of peak reconnection) to $t\Omega_{ci} = 29$. During this time, the electron layer lengthens: the distance from the X line to the end of the electron jet increases from 1 to $8d_i$ and is denoted by the number d (in d_i) given in Figure 3 for each time. The first 1(D–G) and last 5(D–G) distributions are taken from the X line (at $x/d_e = x_0$) and the end of the jet ($x/d_e = x_0 + \sqrt{m_i/m_e}d$), respectively. Distributions 2–4 are evenly spaced between the locations of distributions 1 and 5.

©2015. American Geophysical Union. All Rights Reserved.

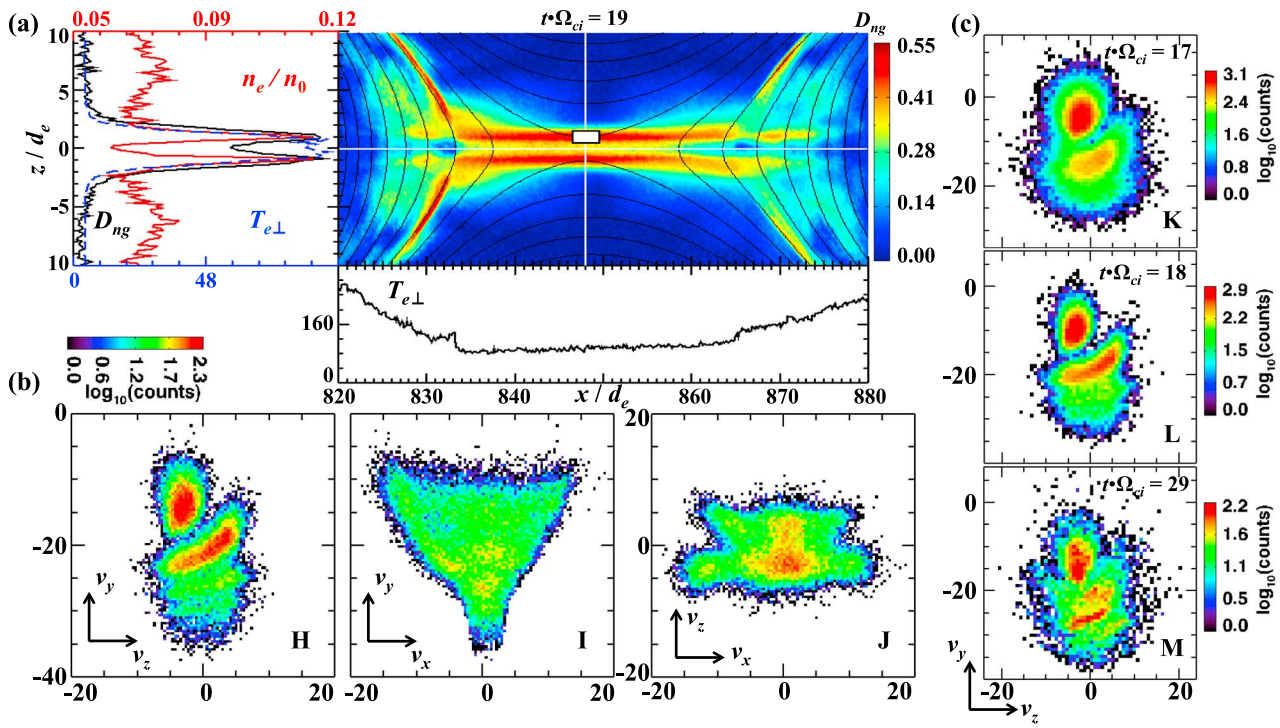

Figure 4. (a) Two-dimensional plot of the degree of electron nongyrotropy, D_{ng}, with vertical cuts (at $x = 848$) of the perpendicular temperature, $T_{e\perp}$ (blue dashes), electron density, n_e (red), and D_{ng} (black), and a horizontal cut (at $z = 0$) of $T_{e\perp}$. Entering the EDR from upstream, $T_{e\perp}$, n_e, and D_{ng} rise sharply in unison. $T_{e\perp}$ increases by a factor of 20 within $2d_e$ from $|z| = 3$ to $|z| = 1$, and grows by another factor of 3 from the X line ($x = 848$) to the outflow jet's end ($x \sim 880$). (b) Reduced electron velocity distribution from $z = 1$ at the location of peak $T_{e\perp}$, n_e, and D_{ng} just above the X line. The distribution in v_z-v_y (H) reveals that the sharp rise in $T_{e\perp}$ and D_{ng} is due to the slanted, gyrophase-bunched populations of accelerated meandering electrons in addition to the zero-bounce population. The distribution in v_x-v_y (I) exhibits the triangular structure characteristic of the X line distribution, though without striations because the slanted populations overlap when projected into the v_x-v_y plane. The two v_z populations in v_x-v_z (J) are roughly centered at the maximum inflow velocities. (c) Time evolution of the gyrobunched populations from $t\Omega_{ci} = 17, 18, 29$, showing that consistent acceleration and heating processes persist as time advances. All distributions are made using a spatial bin size of $3d_e \times 1d_e$.

Distributions from the X line 1(D–G) in Figure 3 all exhibit the characteristic triangular structure. Distributions 1(D–F) show discrete striations in the triangle. After $t\Omega_{ci} = 21$, discrete striations are less visible. Distributions 1F and 1G are more fragmented than distributions 1D and 1E. For example, the striations in distribution 1F are composed of multiple populations, a consequence of the likewise fragmented inflow distributions upstream of the EDR. Fragmentation of inflow distributions may be due to upstream waves and will be the subject of a future publication. Distribution 1G is much less coherent than the X line distributions from earlier times and no longer exhibits distinct striations.

Common to all reconnection phases shown in Figure 3, the distributions downstream from the X line within the electron jet show swirling structures, signatures of EDR-accelerated electrons executing partial cyclotron orbits around B_z. The asymmetry in both v_x and v_y of distributions 2–4 gives rise to a finite P_{exy} whose gradient $\partial P_{exy}/\partial x$ contributes to balancing E_y in the EDR. As the EDR lengthens with time, $|\partial P_{exy}/\partial x|$ decreases. The magnitude of B_z increases gradually with the distance from the X line. At the end of the electron jet, the majority of electrons are magnetized by B_z, as indicated by the mostly gyrotropic distributions 5(D-G).

The nongyrotropic components of distributions at the end of the electron jet 5(D–G) manifest themselves as arc populations. The arc electrons are the most energetic electrons that have been accelerated in the EDR. The maximum speed of the arc electrons increases with time (compare distribution 5D to 5G). Multiple thin and discrete arcs are observed in distribution 5G, likely because the accelerated populations of distribution 1G are fragmented.

The degree of electron nongyrotropy (D_{ng}), vertical cuts (taken at $x = 848$) of D_{ng} (black), the electron density, n_e (red), and $T_{e\perp}$ (blue) on the left, and a horizontal cut of $T_{e\perp}$ (black) are shown in Figure 4a to demonstrate the correlations between these quantities relevant to the EDR heating mechanisms discussed

©2015. American Geophysical Union. All Rights Reserved.

thus far. Because $\mathbf{B} \sim B_x\hat{\mathbf{x}}$ along the vertical cut through the X line, $T_{e\perp} \sim (P_{eyy} + P_{ezz})/2n_e$. $T_{e\perp}$ increases by 20 times within $2d_e$ (blue dashed cut), reaching its maximum at the same location as the n_e and D_{ng} peaks (see vertical cuts in Figure 4a, left), while $T_{e\|}$ ($\sim T_{exx}$) decreases by about a factor of 3 (data not shown). From the X line to the end of the electron jet, the horizontal cut shows that $T_{e\perp}(\sim (P_{exx} + P_{eyy})/2n_e$ since for $z = 0$, $\mathbf{B} \sim B_z\hat{\mathbf{z}}$) further increases by a factor of about 2.4 (from ~ 100 to $\sim 240\ m_e V_A^2$).

The most probable turning points of the meandering electrons in the EDR give rise to the two n_e maxima that are colocated with the extrema of D_{ng}, which measures the departure of a distribution (in the bulk velocity frame) from rotational symmetry around the local magnetic field and is defined as the Frobenius norm of the nongyrotropic part of the pressure tensor normalized by the local thermal energy density [*Aunai et al.*, 2013]. Increased D_{ng} not only occurs in the EDR but also extends along the exhaust side of the separatrices as shown in the 2-D D_{ng} plot; this extension of enhanced D_{ng} continues for tens of d_i away from the X line (data not shown). For the reconnection configurations considered in this paper, enhanced D_{ng} identifies approximately the same spatial regions as the agyrotropy parameter defined previously by *Scudder and Daughton* [2008]. Nongyrotropic electrons have been measured by spacecraft [*Scudder et al.*, 2012; *Chen et al.*, 2008].

The electron distribution from the peak D_{ng} and n_e region right above the X line (marked by the white bin in the D_{ng} plot) is projected onto the v_z-v_y (H), v_x-v_y (I), and v_x-v_z (J) planes in Figure 4b. The v_z-v_y plane is approximately perpendicular to the magnetic field at this location. All of the discrete populations in distribution H are accelerated in the $-y$ direction compared to the inflow distribution shown in greyscale in Figure 1b, and they are bunched in gyrophase. The asymmetry of the distribution in v_y and v_z at the peak D_{ng} location gives rise to a nonzero P_{eyz} whose gradient along z is important for balancing the reconnection electric field in the EDR [*Hesse et al.*, 2011; *Chen et al.*, 2011].

The detailed structure of the distribution can be readily understood by considering the physics behind the discrete striations at the X line. The population with the smallest $|v_y|$ in distribution H (Figure 4b) consists of electrons that have not undergone any bounces in z; since these electrons are inflowing electrons, the population is centered at a negative v_z. The higher-order striations are approximately centered at $v_z = 0$, formed by electrons with more than one z bounce in the vicinity of their turning points. The slant structure of the populations centered at $v_z = 0$ (electrons with positive v_z have lower $|v_y|$ than those with negative v_z) develops because electrons with negative v_z are reflected and spent more time in the EDR, thus gaining more $|v_y|$ than the electrons with positive v_z that have not yet been reflected. Note that since the location of the distribution is above the X line, the electrons with $v_z > 0$ are approaching their turning points, while those with $v_z < 0$ are leaving. For the location of peak D_{ng} below the X line, the slanting slope reverses sign, and the population with the smallest v_y is centered at $v_z > 0$ (not shown).

A characteristic triangular shape is observed in distribution I. The lack of discrete striations is due to the overlapping in v_y of the slanted populations in distribution H. Compared to the grey inflow distribution of Figure 1, distribution J shows the increase of v_z spread without acceleration by the inversion E_z (E_z is insignificant at the edge of the EDR).

The time evolution of the gyrophase-bunched v_z-v_y distribution is shown in Figure 4c. All distributions (K–M) exhibit similar structures as distribution H with higher-order bounce populations at larger $|v_y|$ than the zero-bounce population, indicating similar acceleration and heating processes even for later phases of reconnection such as $t\Omega_{ci} = 29$. All populations gain larger v_y at later times. The discrete populations of distribution M, like distribution 1G (Figure 3), are more fragmented.

4. Summary and Conclusion

We report for the first time the spatiotemporal evolution of electron velocity distributions from the X line to beyond the end of the electron outflow jet applicable to reconnection with symmetric upstream conditions and weak guide fields. Comparison of the EDR distributions with the distributions just upstream and downstream of the EDR enables us to address the open question of electron heating. We demonstrate that the T_e increase is mainly achieved by the cooperation of E_y and B_z forces on meandering EDR electrons. The EDR distributions are highly structured, and the structures indicate consistent acceleration and heating processes occurring throughout the reconnection phases we have examined, implying that wave fluctuations and instabilities only play a minor role, if any, in determining electron heating in the EDR. For the

©2015. American Geophysical Union. All Rights Reserved.

antiparallel simulation discussed in this paper, the amount of electron heating throughout the EDR is about 7 times larger than that due to parallel electric fields upstream from the EDR as shown in Figure 2; for the 3% guide field run (data not shown), the EDR heating was about 5 times larger than that due to upstream parallel electric fields.

The multicomponent nongyrotropic distributions may serve as "smoking-gun" observables to identify the EDR based on spacecraft measurements. The triangular shape and discrete striations may be detectable by the high-resolution electron measurements expected from the upcoming Magnetospheric Multiscale NASA mission.

Acknowledgments
The work at UNH was supported in part by NSF grants PHY-0903923 and AGS-1202537, and NASA grant NNX11AH03G, and at NASA GSFC by the Theory and Modeling Program of the Magnetospheric Multiscale mission. The simulation data are available upon request from the authors. The authors would like to thank S. Wang for the test particle tracing tools used in this study.

The editor thanks Tsugunobu Nagai and an anonymous reviewer for their assistance in evaluating this paper.

References

Aunai, N., M. Hesse, and M. Kuznetsova (2013), Electron nongyrotropy in the context of collisionless magnetic reconnection, *Phys. Plasmas*, *20*, 092903, doi:10.1063/1.4820953.

Bessho, N., L.-J. Chen, J. R. Shuster, and S. Wang (2014), Electron distribution functions in the electron diffusion region of magnetic reconnection: Physics behind the fine structures, *Geophys. Res. Lett.*, *41*, 8688–8695, doi:10.1002/2014GL062034.

Cai, H. J., D. Q. Ding, and L. C. Lee (1994), Momentum transport near a magnetic X line in collisionless reconnection, *J. Geophys. Res.*, *99*(A1), 35–42, doi:10.1029/93JA02519.

Chen, L.-J., et al. (2008), Evidence of an extended electron current sheet and its neighboring magnetic island during magnetotail reconnection, *J. Geophys. Res.*, *113*, A12213, doi:10.1029/2008JA013385.

Chen, L.-J., et al. (2009), Multi-spacecraft observations of the electron current sheet, neighboring magnetic islands, and electron acceleration during magnetotail reconnection, *Phys. Plasmas*, *16*, 056501, doi:10.1063/1.3112744.

Chen, L., W. S. Daughton, B. Lefebvre, and R. B. Torbert (2011), The inversion layer of electric fields and electron phase-space-hole structure during two-dimensional collisionless magnetic reconnection, *Phys. Plasmas*, *18*, 012904, doi:10.1063/1.3529365.

Daughton, W., J. Scudder, and H. Karimabadi (2006), Fully kinetic simulations of undriven magnetic reconnection with open boundry conditions, *Phys. Plasmas*, *13*, 072101, doi:10.1063/1.2218817.

Egedal, J., A. Lê, N. Katz, L.-J. Chen, B. Lefebvre, W. Daughton, and A. Fazakerley (2010), Cluster observations of bidirectional beams caused by electron trapping during antiparallel reconnection, *J. Geophys. Res.*, *115*, A03214, doi:10.1029/2009JA014650.

Egedal, J., W. Daughton, and A. Le (2012), Large-scale electron acceleration by parallel electric fields during magnetic reconnection, *Nat. Phys.*, *8*, 321–324, doi:10.1038/nphys2249.

Fujimoto, K., and R. D. Sydora (2009), Particle description of the electron diffusion region in collisionless magnetic reconnection, *Phys. Plasmas*, *16*, 112309, doi:10.1063/1.3263694.

Hesse, M., S. Zenitani, M. Kuznetsova, and A. Klimas (2009), A simple, analytical model of collisionless magnetic reconnection in a pair plasma, *Phys. Plasmas*, *16*, 102106, doi:10.1063/1.3246005.

Hesse, M., T. Neukirch, K. Schindler, M. Kuznetsova, and S. Zenitani (2011), The diffusion region in collisionless magnetic reconnection, *Space Sci. Rev.*, *160*, 3–23, doi:10.1007/s11214-010-9740-1.

Le, A., J. Egedal, O. Ohia, W. Daughton, H. Karimabadi, and V. S. Lukin (2013), Regimes of the electron diffusion region in magnetic reconnection, *Phys. Rev. Lett.*, *110*, 135004, doi:10.1103/PhysRevLett.110.135004.

Lyons, L. R., and D. C. Pridmore-Brown (1990), Force balance near an X line in a collisionless plasma, *J. Geophys. Res.*, *95*, 20,903–20,909, doi:10.1029/JA095iA12p20903.

Ng, J., J. Egedal, A. Le, W. Daughton, and L.-J. Chen (2011), Kinetic structure of the electron diffusion region in antiparallel magnetic reconnection, *Phys. Rev. Lett.*, *106*, 065002, doi:10.1103/PhysRevLett.106.065002.

Ng, J., J. Egedal, A. Le, and W. Daughton (2012), Phase space structure of the electron diffusion region in reconnection with weak guide fields, *Phys. Plasmas*, *19*, 112108, doi:10.1063/1.4766895.

Scudder, J., and W. Daughton (2008), "Illuminating" electron diffusion regions of collisionless magnetic reconnection using electron agyrotropy, *J. Geophys. Res.*, *113*, A06222, doi:10.1029/2008JA013035.

Scudder, J., R. D. Holdaway, W. S. Daughton, H. Karimabadi, V. Roytershteyn, C. T. Russell, and J. Y. Lopez (2012), First resolved observations of the demagnetized electron-diffusion region of an astrophysical magnetic-reconnection site, *Phys. Rev. Lett.*, *108*, 225005, doi:10.1103/PhysRevLett.108.225005.

Shuster, J., L.-J. Chen, W. S. Daughton, L. C. Lee, K. H. Lee, N. Bessho, R. B. Torbert, G. Li, and M. Argall (2014), Highly structured electron anisotropy in collisionless reconnection exhausts, *Geophys. Res. Lett.*, *41*, 5389–5395, doi:10.1002/2014GL060608.

Speiser, T. W. (1970), Conductivity without collisions or noise, *Planet. Space Sci.*, *18*, 613–622, doi:10.1016/0032-0633(70)90136-4.

©2015. American Geophysical Union. All Rights Reserved.